M. KUBIAK[*,#], W. PIEKARSKA[*], S. STANO[**], Z. SATERNUS[*]

NUMERICAL MODELLING OF THERMAL AND STRUCTURAL PHENOMENA IN Yb:YAG LASER BUTT-WELDED STEEL ELEMENTS

MODELOWANIE NUMERYCZNE ZJAWISK CIEPLNYCH I STRUKTURALNYCH W ELEMENTACH STALOWYCH SPAWANYCH DOCZOŁOWO WIĄZKĄ LASERA Yb:YAG

The numerical model of thermal and structural phenomena is developed for the analysis of Yb:YAG laser welding process with the motion of the liquid material in the welding pool taken into account. Temperature field and melted material velocity field in the fusion zone are obtained from the numerical solution of continuum mechanics equations using Chorin projection method and finite volume method. Phase transformations in solid state are analyzed during heating and cooling using classical models of the kinetics of phase transformations as well as CTA and CCT diagrams for welded steel. The interpolated heat source model is developed in order to reliably reflect the real distribution of Yb:YAG laser power obtained by experimental research on the laser beam profile.

On the basis of developed numerical models the geometry of the weld and heat affected zone are predicted as well as the structural composition of the joint.

Keywords: Laser welding, heat transfer, phase transformations, numerical modelling, Kriging method

Praca dotyczy modelowania numerycznego zjawisk cieplnych i strukturalnych w procesie spawania laserem Yb:YAG z uwzględnieniem ruchu ciekłego materiału w jeziorku spawalniczym. Pole temperatury i pole prędkości ciekłej stali w strefie przetopienia otrzymano z numerycznego rozwiązania równań mechaniki ośrodków ciągłych metodą projekcji Chorina i metodą objętości skończonych. Przemiany fazowe w stanie stałym analizowano podczas nagrzewania i chłodzenia bazując na klasycznych modelach kinetyki przemian fazowych oraz wykresach CTA i CTPc-S. W celu wiarygodnego odzwierciedlenia rzeczywistego rozkładu mocy lasera Yb:YAG opracowano model interpolowany źródła, wykorzystujący badania doświadczalne profilu wiązki laserowej.

Na podstawie opracowanych modeli numerycznych prognozowano geometrię spoiny i strefy wpływu ciepła oraz skład strukturalny złącza.

1. Introduction

One of the most intensively studied and implemented in the industry lasers are diode pumped Yb:YAG lasers with the active element in a shape of a disk, which are characterized by the high efficiency and a low optical quantum defect [1-2]. Many issues concerning this type of laser materials processing are currently under particular investigations in the field of mathematical and numerical modelling as well as experimental research [3-9].

Welding is a complex process which involves interplay between physical phenomena occurring in a wide range of temperatures. Coupled thermal, structural and mechanical phenomena have a direct impact on the quality of welded joint. The problem of controlling welding process and prediction of mechanical properties of welded joints is currently one of the fundamental industrial problems [10, 11]. Therefore, a numerical analysis of thermal phenomena, including phase transformations in the solid state, under different heating and cooling conditions of the joint is important in the prediction of the quality of welded joint.

Many new phenomena occur in the laser welding of steel that are not found in the conventional welding methods. In the case of laser welding a "keyhole" is created with ionised vapour that absorbs the laser beam power. The beam is afterwards transferred to the walls of the "keyhole" forming the fusion zone [12-14]. Moreover, the impact of concentrated heat source on the material causes high temperature gradients as well as different heating and cooling conditions, contributing to the formation of various structures in the weld and heat affected zone, which leads to different mechanical properties [6, 10]. Hardening structures occur in the thermal influence zone due to the impact heating and rapid cooling of a material in the process, even in susceptible to the laser processing, unalloyed and low-alloy constructional steels.

[*]   INSTITUTE OF MECHANICS AND MACHINE DESIGN FOUNDATIONS, CZESTOCHOWA UNIVERSITY OF TECHNOLOGY, 73 DĄBROWSKIEGO STR., 42-200 CZĘSTOCHOWA, POLAND

[**]   WELDING INSTITUTE, 16-18 BŁOGOSŁAWIONEGO CZESŁAWA STR., 44-100 GLIWICE, POLAND

[#]   Corresponding author: kubiak@imipkm.pcz.pl

The main factors characterizing the temperature distribution in the heated element is the amount of heat energy and a method for its delivery to the heated material. A considerable number of studies are focused on the modelling of the case of TEM_{00} Gaussian lasing profiles [4, 5], omitting the effects of non-Gaussian beam distribution [15]. The analysis of solid state laser beam generation process shows that the thermal lensing effect and the spherical aberration occurring in the process change the nature of laser beam power intensity distribution and affects its caustic [16, 17]. Therefore, the use of the Gaussian power distribution models may not be sufficient for the numerical analysis of physical phenomena in Yb:YAG laser welding process.

Moreover, consideration of liquid material motion in the model allows for the analysis of previously neglected phenomena in material melting processes and has a significant impact on the estimated temperature distribution and consequently numerically estimated shape and size of melted zone [5, 8]. There is still a lack of comprehensive models in the literature allowing the analysis of coupled thermal and structural phenomena taking into account the motion of liquid material in the fusion zone.

In this study theoretical model is presented to analyze coupled thermal phenomena and phase transformations in solid state during Yb:YAG butt-welding of S355 steel sheets with the motion of melted material in the fusion zone taken into account. A new interpolation model of laser beam heat source is developed to reliable determination of the real Yb:YAG laser power intensity distribution. The numerical algorithm is implemented into computer solver to predict the geometry of the weld and heat affected zone as well as the structural composition of the joint. Selected results of computer simulations are verified by experimental research performed using Yb:YAG disk laser.

2. Experimental research

The research is performed using Trumpf D70 laser head combined with TruDisk 12002 disk laser (Fig. 1a). Basic parameters of the laser beam are obtained using Prometec UFF100 beam analyzer (Fig. 1b), a diagnostic device for measuring high power lasers profile. The precise needle shifting system allows the scan of the beam along its cross-section for several different section planes, allowing three-dimensional imaging of the density distribution of the laser power and two-dimensional profile of the laser beam. The laser used

in the research has maximum power of 12kW. The fiber with a diameter $dLLK$=400μm is used in experimental research. The welding head is equipped with a collimator lens having a focal length f_c =200 mm and a focusing lens having a focal length of f =400 mm, therefore double magnification of the optical system is achieved and a laser beam diameter d =0.8 mm.

The analysis of Yb:YAG laser power distribution is performed at the continuous power 900W of the laser beam due to the limitations of the resistance of measuring needle and the detector of UFF100 system. Each measurement is the mean value of seven scans of the laser beam in the testing plane, computed automatically by Prolas computer software program supporting UFF100 analyzer. Figures 2-3 present

Fig. 2. Experimentally obtained percentage distribution of Yb:YAG laser beam power at beam focusing z=0

Fig. 3. Experimentally obtained percentage distribution of Yb:YAG laser beam power at beam focusing z=5 mm
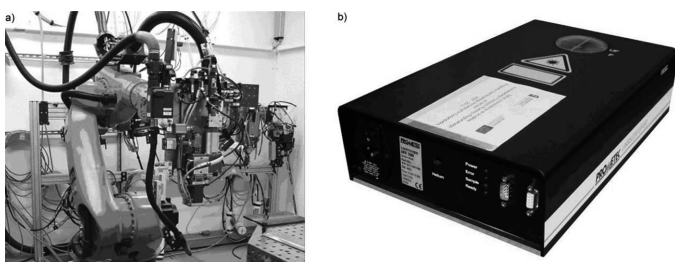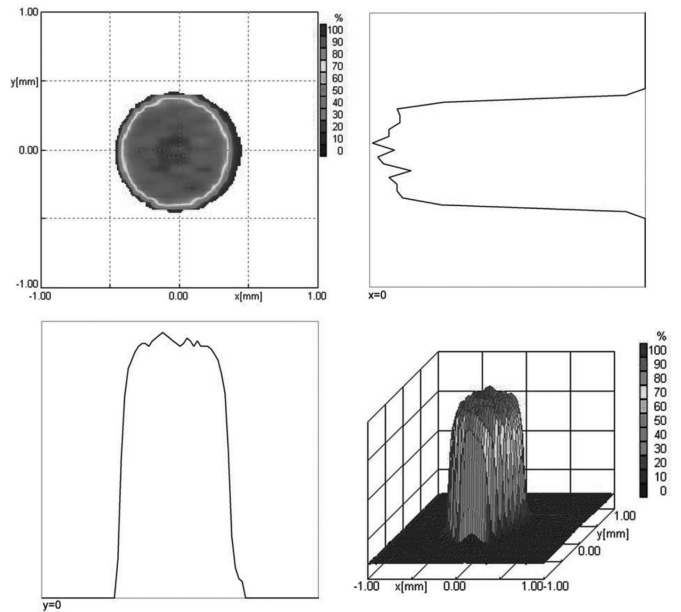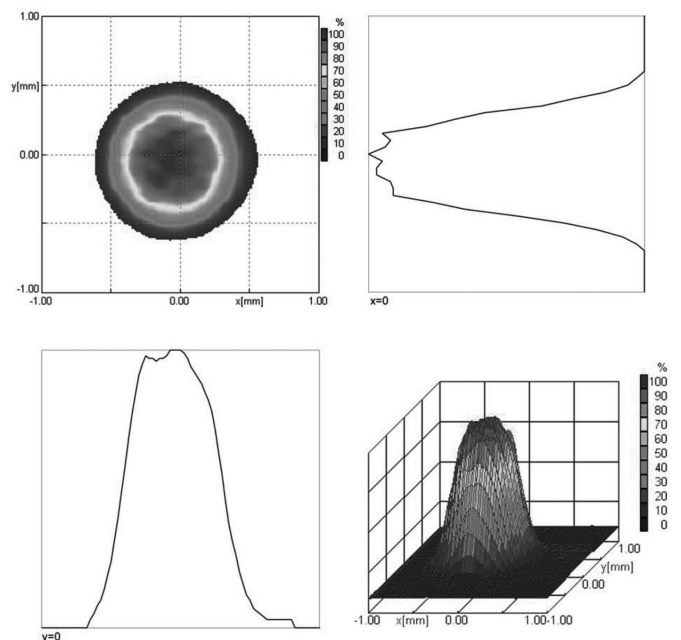

Fig. 1. Laser welding station: a) laser disk TruDisk 12002 with D70 laser head mounted on the wrist of KUKA industrial robot and b) laser beam analyzer UFF100

percentage distribution of Yb:YAG laser beam power for two chosen beam focusing positions (z=0 and z=5 mm) in the observation window 2×2 mm with distributions of beam power at the central axes (x=0 and y=0). Figure 4 illustrates laser beam 3D caustic created by measuring radius w_x and w_y, in the plane (x, y), defined as the dependence of the moment of the second order power density distribution in accordance with standard PN-EN ISO 11146.

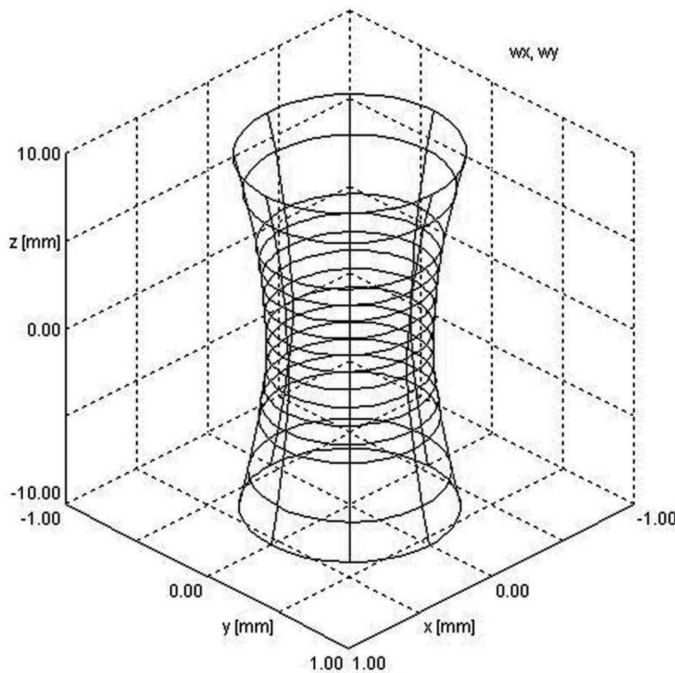Fig. 5. The cross section of Yb:YAG laser butt-welded joint

Fig. 4. Laser beam 3D caustic created by measuring the radius w_x and w_y, according to PN-EN ISO 11146 norm

Real single laser butt-welding process is performed in order to compare characteristic zones of welded joint (melted zone and heat affected zone) with numerically estimated temperature distributions. Steel sheets made of S355 steel with dimensions 250×50×5 mm are butt-welded using Yb:YAG laser (Fig. 1a). Process parameters shown in Table 1 are used in the experiment.

TABLE 1

Laser beam butt-welding process parameters

Welding speed	1 m/min
Laser power	3000 W
Beam focusing	z=0
Angle of incidence of the laser beam on the surface of the joint	0°
Sheets fit-up	g≈0 mm (without gap)

Figure 5 shows the macrostructure of the cross section of butt-joint made by Yb: YAG laser with parameters shown in Table 1.
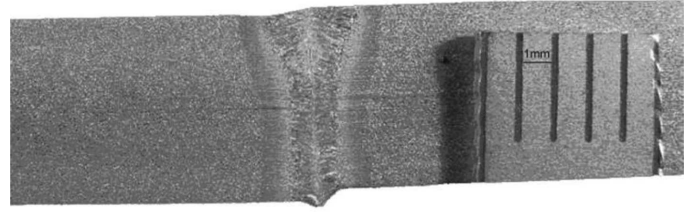
3. Theoretical approach

In a single laser beam welding highly concentrated heat source melts the workpiece causing significant evaporation of the material in heat source activity zone and creating the "keyhole". Heat transfer in welded joint depends on the amount and distribution of heat energy supplied to the workpiece, welding speed and the motion of a liquid material in the welding pool. Phase transformations due to melting, solidification and evaporation as well as phase transformations in solid state are taken into account in theoretical investigations. The region between solidus and liquidus temperatures (mushy zone) is treated as the porous medium (Darcy's model). At boundaries of the workpiece heat loss due to convection, radiation and evaporation is assumed. Sketch of considered system is illustrated in Figure 6.
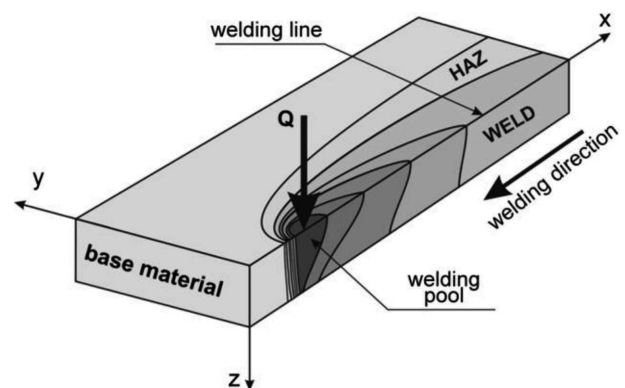

Fig. 6. Schematic sketch of laser beam welding

3.1. Heat source model

Ordinary Kriging method [18, 19] in the form of point Kriging is used for a precise description of solid state laser power intensity distribution. Kriging interpolation at a point (x, y) is a linear combination of observations in basic points (the real power distribution). The estimate is a function of the weighted average:

$$\tilde{f}(x, y) = \sum_{i=1}^{n} w_i f(x_i, y_i) \tag{1}$$

where w_i are weight coefficients assigned to particular observations, $f(x_i, y_i)$ is the real value of the function (variable) at the measured point, n is the number of sampling points that are considered in estimating of the variable within the circle of radius r_k from estimated point.

Coefficients w_i are calculated on the basic of Kriging system of equations, as follows:

$$\begin{bmatrix} 0 & \gamma(h_{12}) & \gamma(h_{13}) & \dots & \gamma(h_{1n}) & 1 \\ \gamma(h_{21}) & 0 & \gamma(h_{23}) & \dots & \gamma(h_{2n}) & 1 \\ \gamma(h_{31}) & \gamma(h_{32}) & 0 & \dots & \gamma(h_{3n}) & 1 \\ \dots & \dots & \dots & \dots & \dots & \dots \\ \gamma(h_{n1}) & \gamma(h_{n2}) & \gamma(h_{n3}) & \dots & 0 & 1 \\ 1 & 1 & 1 & \dots & 1 & 0 \end{bmatrix} X \begin{bmatrix} w_1 \\ w_2 \\ w_3 \\ \dots \\ w_n \\ \lambda \end{bmatrix} = \begin{bmatrix} \gamma(d_1) \\ \gamma(d_2) \\ \gamma(d_3) \\ \dots \\ \gamma(d_n) \\ 1 \end{bmatrix} \quad (2)$$

where $\gamma(h_{ij})$ are the values of theoretical semivariogram at the distance h_{ij} between basis points in the observation set, $\gamma(d_i)$ are the values of theoretical semivariogram at the distance d_i between observed point and i-th basic point, λ is Lagrange multiplier.

Theoretical semivariogram is generally unknown, therefore values of function $\gamma(h_{ij})$ and $\gamma(d_i)$ are approximated by a linear function $\gamma(h) = C_0 + Sh$, in which the semivariogram tends to sill S at $h \rightarrow \infty$, while C_0 is a function discontinuity (nugget effect). Coefficients S and C_0 are estimated using empirical semivariogram and sample variance Var. The volumetric heat source power distribution is calculated assuming the linear decrease of energy intensity with material penetration:

$$Q_V(x, y, z) = \eta Q_S \tilde{f}(x, y)\left(1 - \frac{z}{s}\right) \quad (3)$$

where η is the absorption coefficient, $Q_S = \alpha P/\pi\omega_0^2 s$ is the laser power per unit area [W/m^2], P is pumped power [W], ω_0 is a radius of the beam [m], s is the heat source penetration depth [m], α is a heat source coefficient (for the cone like shape of the volume of a heat source the distribution $\alpha = 3$).
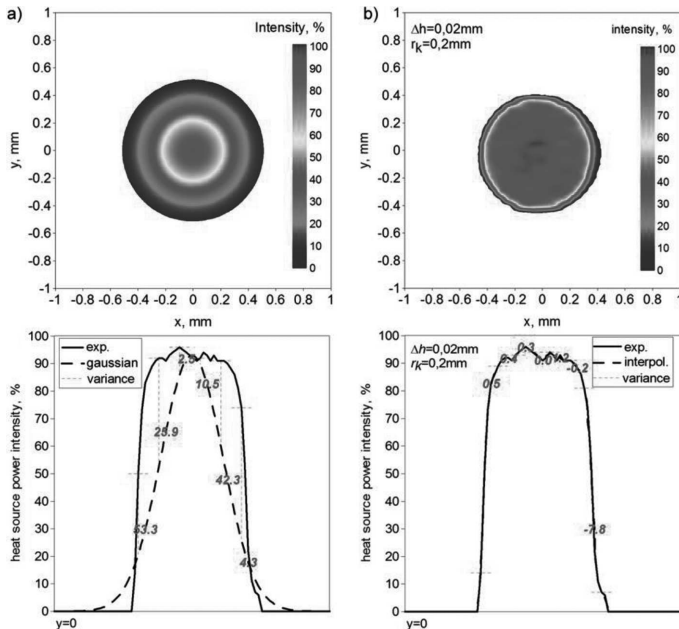

Fig. 7. Percentage distribution of laser power described by a) Gaussian and b) interpolated models

3.2. Thermal phenomena

Differential governing equations used for the analysis of thermal phenomena in laser welding process consist of mass, momentum and energy conservation equations, formulated as follows:

$$\frac{\partial \rho}{\partial t} + \frac{\partial}{\partial x_i}(\rho v_i) = 0 \quad (4)$$

$$\frac{\partial(\rho v_i)}{\partial t} + \frac{\partial}{\partial x_j}(\rho v_i v_j) = -\frac{\partial p}{\partial x_i} + \frac{\partial}{\partial x_j}\left(\mu\frac{\partial v_i}{\partial x_j}\right) + \mathbf{g}\beta_T\left(T - T_{ref}\right) - \frac{\mu}{\rho K}v_i \quad (5)$$

$$\frac{\partial}{\partial x_i}\left(\lambda\frac{\partial T}{\partial x_i}\right) = C_{ef}\left(\frac{\partial T}{\partial t} + v_i\frac{\partial T}{\partial x_i}\right) - Q_V \quad (6)$$

where ρ is a density [kg/m^3], $\mathbf{g}$ is acceleration of gravity, β_T is a volume expansion coefficient due to heating [1/K], T_{ref} is a reference temperature [K], μ is a dynamic viscosity [kg/ms], K is porous medium permeability described by Carman-Kozeny equation [5], $T = T(x_i, t)$ is temperature [K] at a point x_i, v_i is a velocity vector [m/s], $\lambda = \lambda(T)$ is a thermal conductivity, $C_{ef} = C_{ef}(T)$ is an effective heat capacity with latent heat of fusion, evaporation and latent heat of phase transformations in solid state taken into account.

Initial conditions and boundary conditions complete above governing equations. Equation (5) is completed by initial condition $t = 0$: $\mathbf{v} = 0$ and boundary conditions implemented at the welding pool boundary determined by solidus temperature ($T_{ref} = T_S$), described as follows:

$$\Gamma: \quad \mathbf{v}|_{\Gamma} = 0, \quad \tau_s = \mu\frac{\partial \mathbf{v}}{\partial n} = \frac{\partial \gamma}{\partial T}\frac{\partial T}{\partial s} \quad (7)$$

where τ_s is Marangoni shear stress in the direction tangent to the surface, γ is surface tension coefficient.

Equation (6) is completed by initial condition: $t = 0$: $T = T_0$ and boundary conditions, taking into account heat loss due to convection, radiation and evaporation:

$$\Gamma: \quad -\lambda\frac{\partial T}{\partial n} = \alpha(T|_{\Gamma} - T_0) + \varepsilon\sigma(T^4|_{\Gamma} - T_0^4) - q_o + q_v \quad (8)$$

where α is convective coefficient [W/m^{2}K], ε is radiation coefficient, and σ is Stefan-Boltzmann constant. Element q_o is the heat flux towards the top surface of the welded element ($z = 0$) in the source activity zone, while q_v represents heat loss due to material evaporation in area where $T \geqslant T_L$, $\check{A}$ is a boundary of analyzed domain.

Changes in material state during steel processing require appropriate description of phase transformations in theoretical considerations. Temperature field during material melting and solidification is affected by the latent heat of fusion. Macro models describing solidification process for both pure metals [20-23] and alloys [24-28] can be found in the literature. Mostly, one domain approach is used with fuzzy solidification front in the model where latent heat is included into effective heat capacity.

In this study latent heat of fusion [26, 28], evaporation [5, 8, 12] and latent heat of phase transformations in solid state [29-31] are considered in the capacity model. Effective heat capacity is defined assuming linear approximation of solid fraction in the mushy zone and liquid fraction in liquid-gas

region as well as the increase of a volumetric fraction of i-th phase in the solid state:

$$C_{ef}(T) = \begin{cases} \rho_S c_S + \sum_i \rho_S H_i^{\eta_i} \dfrac{d\eta_i(T)}{dT} & \text{for} \quad T \in \left[T_{st}^i; T_{fi}^i\right] \\ \rho_S c_S & \text{for} \quad T \notin \left(T_{st}^i; T_{fi}^i\right) \cup T < T_S \\ \rho_{SL} c_{SL} + \rho_S \dfrac{H_L}{T_L - T_S} & \text{for} \quad T \in [T_S; T_L] \\ \rho_L c_L & \text{for} \quad T \in [T_L; T_b] \\ \rho_L c_L + \dfrac{\rho_L H_b}{T_{max} - T_b} & \text{for} \quad T \in [T_b; T_{max}] \end{cases}$$

(9)

where c is a specific heat [J/kgK], subscripts S and L denote solid and liquid state, T_{st}^i and T_{fi}^i are start and finish temperatures of each phase transformation in solid state [K], $H_i^{\eta_i}$ is a latent heat of i-th phase transformation [J/kg], η_i is a volumetric fraction of i-th phase (latent heats of austenite into ferrite $H_{A \to F}$, pearlite $H_{A \to P}$, bainite $H_{A \to B}$ and martensite $H_{A \to M}$ transformation are assumed according to [29, 31]), T_S and T_L are solidus and liquidus temperatures respectively [K], H_L is a latent heat of fusion [J/kg], T_b is the boiling point of steel [K], T_{max} is the maximum temperature of thermal cycle, H_b is a latent heat of evaporation [J/kg].

The product of density and specific heat in the mushy zone is calculated with assumption of linear approximation of solid fraction:

$$c_{LS}\rho_{LS} = c_S \rho_S f_S + c_L \rho_L (1 - f_S) \qquad (10)$$

where $f_S \in [0; 1]$ is the solid fraction.

3.3. Phase transformation in solid state

Phase transformations in solid state are calculated on the basis of classic mathematical models of kinetics of phase transformations as well as CHT and CCT diagrams determined experimentally [32, 33]. The analysis of phase transformations in solid state is performed for heating and cooling processes for S355 steel, with chemical composition: 0.19 C, 1.05 Mn, 0.2 Si, 0.08 Cr, 0.11 Ni, 0.006 Al, 0.028 P, 0.02 S [%].

Phase transformations during heating are calculated on the basis of Johnson-Mehl-Avrami (JMA) equation taking into account the influence of heating rates on austenitization temperatures $Ac_1(t)$ and $Ac_3(t)$ (CHT diagram).

$$\tilde{\eta}_A(T, t) = \eta_{(.)}(1 - \exp(-b\,t^n)) \qquad (11)$$

where $\eta_{(.)}$ is a sum of volumetric fractions of base material structure ($\eta_{(.)} = 1$), coefficients $b = b(\Theta)$ and $n = n(\Theta)$ are determined by starting ($\eta_s = 0.01$) and final ($\eta_f = 0.99$) conditions for phase transformation as follows

$$b(T) = -\frac{\ln(\eta_f)}{(t_s)^{n(T)}}, \quad n(T) = \frac{\ln\left(\ln\left(\eta_f\right)/\ln\left(\eta_s\right)\right)}{\ln\left(t_s/t_f\right)} \qquad (12)$$

where t is a time, $t_s = t_s(T_{sA})$ and $t_f = t_f(T_{fA})$ are phase transformation start and final times, T_{sA} i T_{fA} are start and final temperatures.

In the case of incomplete austenitization (maximum temperature of thermal cycle is found between austenitization temperatures), aggregated fractions of phases arising during cooling are assumed as a sum of fractions transformed from

austenite and reminder untransformed (base material) structure.

The volumetric fractions of phases forming from austenite during cooling are determined by temperatures and cooling rates in temperature range [800÷500] °C. A fraction of a new phase growth for diffusive transformations (austenite into ferrite, pearlite and bainite) is determined by JMA formula:

$$\eta_{(.)}(T, t) = \eta_{(.)}^{\%} \tilde{\eta}_A \left(1 - \exp\left(-b\left(t(T)\right)^n\right)\right),$$

$$\underline{\eta}_A - \sum_{k=1}^{4} \eta_k \geqslant 0, \quad \sum_{k=1}^{5} \eta_k^{\%} = 1 \qquad (13)$$

where $\eta_{(.)}^{\%}$ is the maximal phase fraction for determined cooling rate, estimated on the basis of CCT diagram, $\underline{\eta}_A$ is the austenite fraction formed due to heating, while η_k is a phase fraction formed before calculated phase transformation during cooling. Coefficients b and n are also calculated from formula (12).

Volumetric fraction of martensite (ηM) is estimated using Koistinen-Marburger (KM) equation

$$\eta_M(T) = \eta_{(.)}^{\%} \tilde{\eta}_A \left(1 - \exp\left(-k\left(M_s - T\right)^m\right)\right), \quad T \in \left[M_s, M_f\right] \qquad (14)$$

Coefficient k depends on martensite phase start and final temperatures (M_s and M_f) determined also basing on CCT diagram

$$k = -\frac{\ln(\eta_S)}{M_s - M_f} = -\frac{\ln(0.01)}{M_s - M_f} \qquad (15)$$

CHT and CCT diagrams of S355 steel used in the analysis as well as final fractions of structure constituents are obtained on the basis of dilatometric research performed on DIL805 dilatometer produced by Bähr Thermoanalyse GmbH, equipped with a LVDT measuring head, with a theoretical resolution of 0.057 μm. In dilatometric analysis a constant austenitization temperature $T_A = 1100°$C was assumed and different heating and cooling rates, simulating thermal cycles in welding. Obtained CHT and CCT diagrams as interpolation functions [33] are implemented into numerical algorithms with diagram of fractions of structural constituents (Fig. 8).
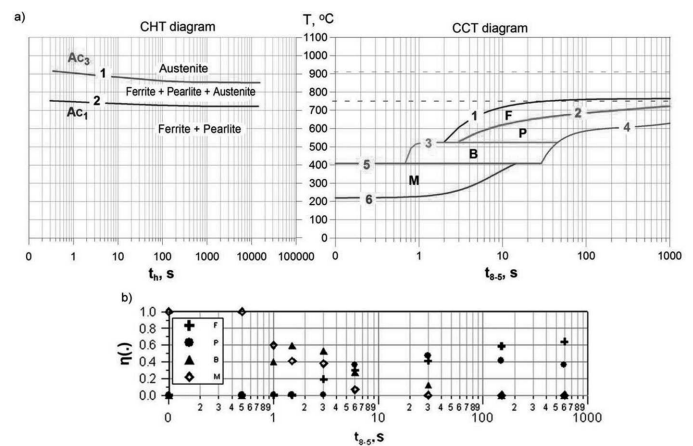

Fig. 8. Interpolated a) CHT and CCT diagrams with b) final fractions of structure constituents for S355 steel

4. Results and disscusion

Differential equations are numerically solved using projection method with finite volume method (FVM) [34]. The spatial variables are discretized using staggered grid to avoid odd-even decoupling between the pressure and velocity. Numerical algorithms are implemented into computer solver using ObjectPascal programming language. Computer simulations of the Yb:YAG laser welding process are performed for a metal sheet made of S355 steel. The sheet dimensions are 250 mm in length, 50 mm in width, with a thickness of 5 mm. The analyzed domain is discretized by a staggered grid with the spatial step set to 0.1 mm. Thermo-physical parameters used in calculations are summarized in Table 2.

The numerical analysis is made using interpolated heat source model. Process parameters are set to: laser beam power $Q = 3000$ W, laser head movement speed $v = 1$ m/min with the focusing point on the top surface of heated element ($z = 0$) and heat source penetration depth $s = 6$ mm.

TABLE 2

Thermophysical parameters used in calculations

Nomenclature	Symbol	Value
Solidus temperature	T_S,	1750 K
Liquidus temperature	T_L	1800 K
Boiling point	T_b	3010 K
Ambient temperature	T_0	293 K
Specific heat of solid phase	c_S	650 J kg^{-1}K^{-1}
Specific heat of liquid phase	c_L	840 J kg^{-1}K^{-1}
Density of solid phase	ρ_S	7800 kg m^{-3}
Density of liquid phase	ρ_L	6800 kg m^{-3}
Latent heat of fusion	H_L	270×10^3 J kg^{-1}
Latent heat of evaporation	H_b	76××10^5 J kg^{-1}
Latent heat of phase transformations	$H_{A \to F}$ $H_{A \to P}$ $H_{A \to B}$ $H_{A \to M}$	8×10^4 J/kg 9×10^4 J/kg 11.5×10^4 J/kg 11.5×10^4 J/kg
Thermal conductivity of solid phase	λ_S	45 W m^{-1}K^{-1}
Thermal conductivity of liquid phase	λ_L	35 W m^{-1}K^{-1}
Convective heat transfer coefficient	α	50 W m^{-2}K^{-1}
Boltzmann's constant	σ	5.67x10^{-8} W m^{-2}K^{-4}
Thermal expansion coefficient	β_T	4.95x10^{-5} K^{-1}
Surface radiation emissivity	ε	0.5
Dynamic viscosity	μ	0.006 kg m^{-1}s^{-1}
Solid particle average diameter	d_0	0.0001 m

Figure 9 shows the temperature field at the top surface (from the face of the weld). The welding pool boundary is represented by a solid line (solidus isotherm), whereas the boundary of heat affected zone is pointed out by a dashed line ($T_g = Ac_1 \approx 1000$K). Temperature field and melted material velocity field are presented in the longitudinal section (Fig. 10) in the middle of heat source activity zone ($y = 0$)

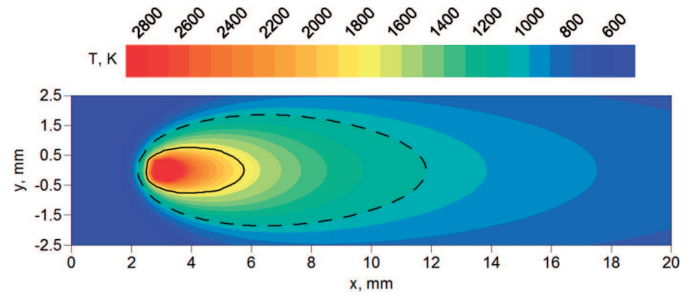and in the cross section (Fig. 11) of the joint, at the distance x=3.2 mm.

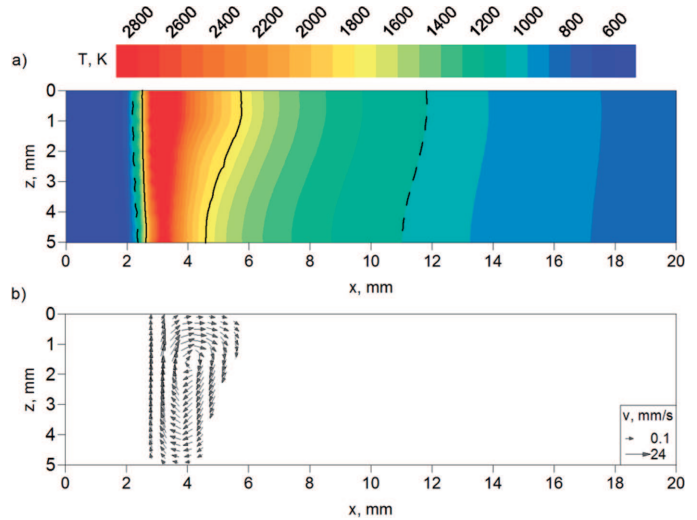Fig. 9. Temperature distribution at the top surface ($z = 0$) of laser welded joint (form the face of the weld)

Fig. 10. Distribution of a) temperature and b) melted material velocity in the longitudinal section (y=0) of laser welded joint
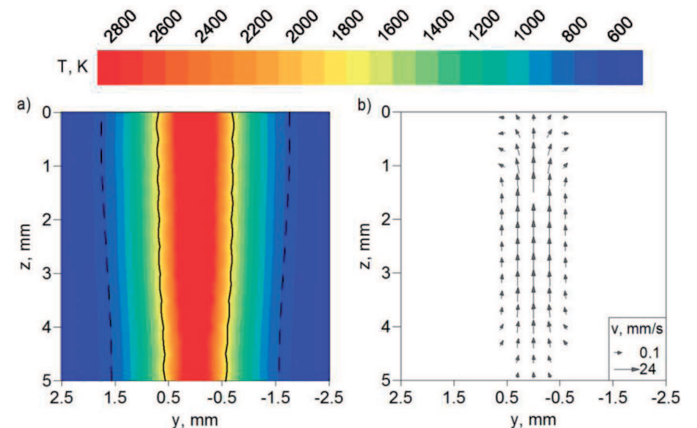

Fig. 11. Results of calculations in the cross-section of welded joint, temperature field and b) melted material velocity field

Figure 12 presents thermal cycles for chosen points at the top surface of the weld. In this figure solidus, liquidus and boiling temperatures are marked as well as temperature range [800°C; 500°C] where cooling rates are determined for the analysis of phase transformations in solid state. The kinetics of phase transformations in solid state is calculated on the basis of obtained thermal cycles. Figure 13 presents the kinetics

of phase transformations for two chosen thermal cycles at the top surface of the weld.
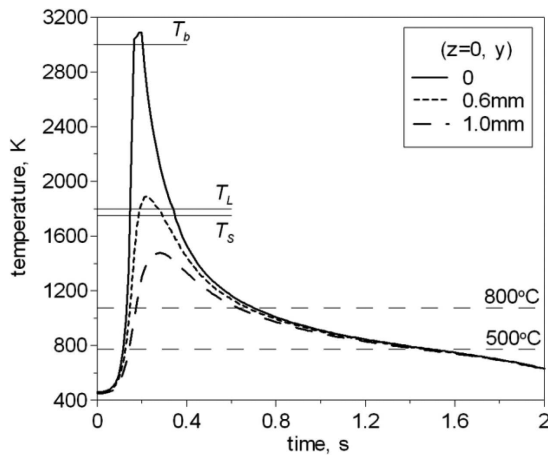

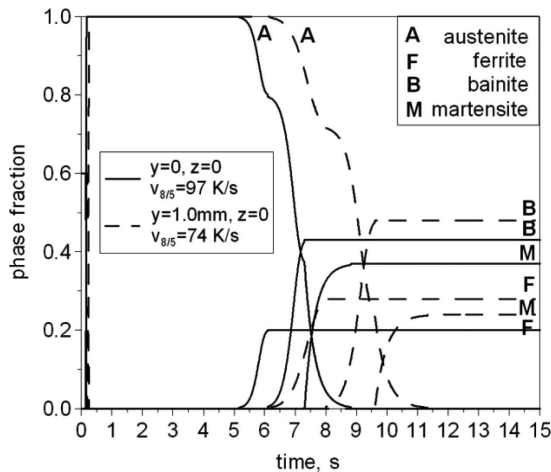Fig. 12. Chosen thermal cycles at the top surface of welded joint

Fig. 13. Kinetic of phase transformations for chosen temperature history
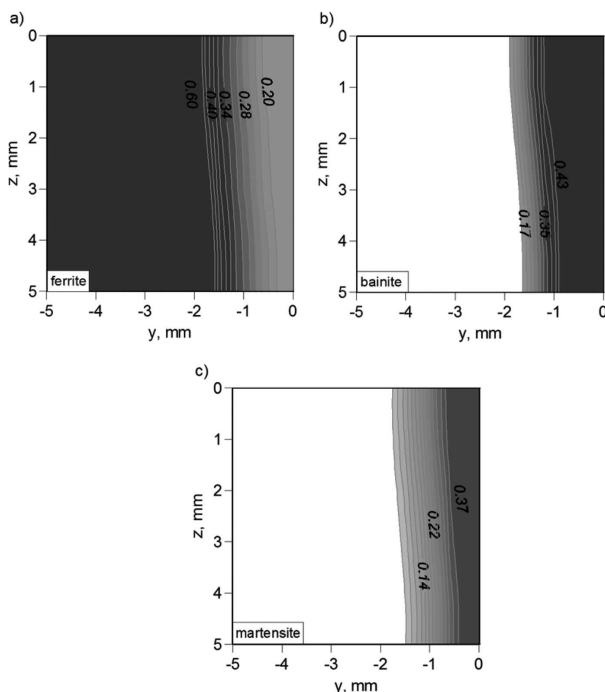

Fig. 14. Predicted structure composition in the cross section of Yb:YAG laser welded joint

The prediction of structure composition is performed for each thermal cycle in the weld and HAZ. Estimated ferrite, bainite and martensite fractions in the structure composition of Yb:YAG laser butt-welded joint are presented in Figure 14.

Figure 15 shows the comparison between results of Yb:YAG laser welding simulation and the macroscopic picture of the cross section of the weld with marked fusion zone and HAZ boundary.
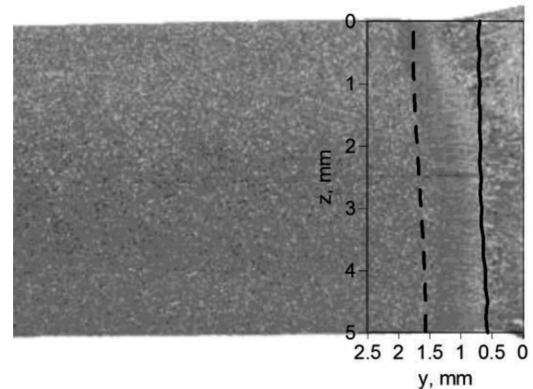

Fig. 15. Comparison between chosen results of calculations with the macroscopic picture of the real laser welded joint

5. Conclusions

This paper presents numerical analysis of thermal phenomena and structural phenomena in Yb:YAG laser beam butt-welding of S355 steel. Three-dimensional numerical model of temperature field in welded joint takes into account the motion of liquid metal in the welding pool and latent heat associated with the material's state change as well as latent heat generated during phase transformations in solid state. Interpolated Yb:YAG laser heat source is developed on the basis of experimental studies of the laser beam profile for the precise mapping of the laser beam power intensity distribution. Chosen results of computational analysis are then compared to experimental results in order to evaluate the suitability of the model in practical applications.

The following conclusions can be made from this study:
– Performed comparison of the heat source power distribution models (Fig. 7) shows that the variance between the distribution determined by Gaussian model and the real distribution of Yb:YAG laser power is significant. Application of Kriging method allows using experimental studies in developed numerical algorithms.
– Calculated temperature field in the cross section of the joint (Fig. 11) allows for the determination of the fusion zone and heat affected zone geometry. It is observed that melted material velocity vectors reaches maximum in the middle of heat sources activity zone (Fig. 10 and Fig. 11).
– On the basis of obtained kinetics of phase transformations in solid state (Fig. 13) it can be noticed that high cooling rates occurring in this process contribute to the rise of martensite volumetric fraction and in consequence the level of joint hardening. As shown in Figure 14, laser welded joint after solidification is rapidly cooled to the ambi-

ent temperature. Predicted martensite fraction for chosen process parameters is up to 37% in the welding line.

– It can be observed that numerically estimated fusion zone and heat affected zone well agree with experimentally obtained macroscopic picture of the cross section of laser welded joint.

Finally, it can be concluded that developed comprehensive computational model allows to assess the geometry and structural composition of Yb:YAG laser welded joint in terms of different process parameters, including different beam intensity distributions for chosen beam focusing. Presented solutions may be useful in industrial practice.

REFERENCES

[1] F. Bachmann, P. Loosen, R. Poprawe, Springer Series in Optical Sciences 128, Springer (2007).

[2] R. Brockmann, D. Havrilla, Laser Technik Journal. **6**, 26 (2009).

[3] T.Y. Fan, IEEE J Quantum Elect. **29,** 1457 (1993).

[4] D. Gery, H. Long, P. Maropoulos, J Mater Process Tech. **167**, 393 (2005).

[5] L. Han, F.W. Liou, Int J Heat Mass Trans. **47**, 4385 (2004).

[6] W. Piekarska, M. Kubiak, Z. Saternus, Arch Metall Mater. **57**, 1219 (2012).

[7] A. Lisiecki, Arch Metall Mater. **59**, 1625 (2014).

[8] W. Piekarska, M. Kubiak, Appl Math Model. **37**, 2051 (2013).

[9] P. Lacki, K. Adamus, K. Wojsyk, M. Zawadzki, Z. Nitkiewicz, Arch Metall Mater. **56**, 455 (2011).

[10] C. Daves, Laser Welding: A practical guide; Abington Publishing (1992).

[11] M. Węglowski, S. Stano et al., Mater Sci Forum. **638-642**, 3739 (2010).

[12] X. Jin, L. Li, Y. Zhang, J Phys. D: Appl Phys. **35**, 2304 (2002).

[13] D.V Bedenko, O.B Kovalev, I.V. Krivtsun, J Phys D: Appl Phys. **43**, 105501 (2010).

[14] M. Beck, P. Berger, H. Hugel, J Phys D: Appl Phys. **28**, 2430 (1995).

[15] X. Song, B. Li, Z. Guo, S. Wang, D. Cai, J. Wen, Optics Communications. **282**, 4779 (2009).

[16] H.S. Kim, J.M. Yang, J Korean Phys Soc. **55**, 1425 (2009).

[17] W. Xie, S-C. Tam, Y-L. Lam, J. Liu et al., Appl Optics. **39**, 5482 (2000).

[18] M.A. Oliver, R. Webster, Int J Geogr Inf Syst. **4**, 313 (1990).

[19] S. Sakata, F. Ashida, M. Zako, Computational Methods in Applied Mechanical Engineering **192**, 923 (2003).

[20] F. Yigit, L.G. Hector, J Therm Stresses. **25**, 663 (2002).

[21] T. Skrzypczak, E. Węgrzyn-Skrzypczak, Int J Heat Mass Trans. **55**, 4276 (2012).

[22] M.A. Rady, V.V. Satyamurty, A.K. Mohanty, Heat Mass Transfer. **32**, 499 (1997).

[23] T. Skrzypczak, Arch Metall Mater. **57**, 1189 (2012).

[24] Nedjar, Comput Struct. **80**, 9 (2002).

[25] L. Sowa, Archives of Foundry Engineering. **11**, 199 (2011).

[26] J.M. Dowden, The mathematics of thermal modeling, Taylor & Francis Group, USA (2001).

[27] L. Sowa, A. Bokota, Arch Metall Mater. **57**, 1163 (2012).

[28] E. Majchrzak, B. Mochnacki, J.S. Suchy, J Theor Appl Mech. **46**, 257 (2008).

[29] K. Mundra, T. DebRoy, Metall Trans B. **24B**, 145 (1993).

[30] A. Bokota, T. Domański, Arch Metall Mater. **52**, 277 (2007).

[31] S. Serajzadeh, J Mater Process Tech. **146**, 311 (2004).

[32] T. Domański, A. Bokota, Arch Metall Mater. **56**, 325 (2011).

[33] W. Piekarska, M. Kubiak, Z. Saternus, Arch Metall Mater. **58**, 1391 (2013).

[34] S.V. Patankar, Numerical heat transfer and fluid flow, Taylor & Francis, USA (1990).